

Intracellular mechanical drugs induce cell cycle altering and cell death

María Isabel Arjona<sup>1\*</sup>, Marta Duch<sup>1\*</sup>, Alberto Hernández-Pinto<sup>2\*</sup>, Patricia Vázquez<sup>2\*</sup>, Juan Pablo Aguil<sup>1</sup>, Rodrigo Gómez-Martínez<sup>1</sup>, Mariano Redondo-Horcajo<sup>2</sup>, Ezhil Amirthalingam<sup>3</sup>, Lluïsa Pérez-García<sup>3,4</sup>, Teresa Suárez<sup>2#</sup> and José A. Plaza<sup>1#</sup>

\* These authors contribute equally

# Corresponding authors

Affiliations: <sup>1</sup>Instituto de Microelectrónica de Barcelona, IMB-CNM (CSIC), Campus UAB, 08193, Cerdanyola del Vallès, Barcelona, Spain. <sup>2</sup>Centro de Investigaciones Biológicas Margarita Salas, CIB (CSIC), 28040, Madrid, Spain. <sup>3</sup>Departament de Farmacologia, Toxicologia i Química Terapèutica and Institut de Nanociència i Nanotecnologia (IN2UB), Universitat de Barcelona, 08028, Barcelona, Spain. <sup>4</sup>School of Pharmacy, University of Nottingham, NG7 2RD, UK.

**keywords:** nanomaterials, biomaterials, silicon chips, mechanobiology, cell cycle, nanomedicine

This article has been accepted for publication and undergone full peer review but has not been through the copyediting, typesetting, pagination and proofreading process, which may lead to differences between this version and the [Version of Record](#). Please cite this article as [doi: 10.1002/adma.202109581](https://doi.org/10.1002/adma.202109581).

This article is protected by copyright. All rights reserved.

Current advances in materials science have demonstrated that extracellular mechanical cues can define cell function and cell fate. However, a fundamental understanding of the manner in which intracellular mechanical cues affect cell mechanics remain elusive. We here describe how intracellular mechanical hindrance, reinforcement and supports interfere with the cell cycle and promote cell death. Reproducible devices with highly controlled size, shape and with a broad range of stiffness were internalized in HeLa cells. Once inside, they induced characteristic cell cycle deviations and promoted cell death. Device shape and stiffness were the dominant determinants of mechanical impairment. Device structural support to the cell membrane and centring during mitosis maximized their effects, preventing spindle centring and correct chromosome alignment. Nanodevices reveal that the spindle generated forces larger than 114 nN which overcome intracellular confinement by relocating the device to a less damaging position. By using intracellular mechanical drugs, this work provides a foundation to defining the role of intracellular constrains on cell function and fate, with relevance to fundamental cell mechanics and nanomedicine.

## Introduction

It is increasingly clear that physical and chemical features of the cell are both fundamental to function and development. The cell's cytoskeleton, composed of microtubules, actin filaments and intermediate filaments, is an active structure associated with mechanical function and is thus involved in many fundamental processes during the cell cycle<sup>1,2</sup>. In physical terms, the combination of cell membrane-cortex system and cytoskeleton constitutes a mechanical system whose stability is based on a force balance between compression and tensile load-bearing components<sup>1</sup>. Any physical perturbation of this cellular mechanical system elicits a redistribution of forces and rearrangement of mechanical elements that can be disruptive<sup>3</sup>. Thus, it is not surprising that multiple chemical drugs for research and therapeutics target to alter the cellular mechanical performance. Anti-cancer drugs such as paclitaxel or colchicine affect the microtubules, provoking mitotic catastrophe to cause cell death<sup>4,5</sup>. Other compounds, including cytochalasin B, cytochalasin D and latrunculin A disrupt actin filaments, also disturbing cell function and growth<sup>6</sup>.

Intracellular mechanical cues induced by physiological internalization of large objects can also alter the redistribution of forces and the rearrangement of mechanical elements. Indeed, during entosis (the engulfment of one living cell by another) cytokinesis in the engulfing cell is perturbed, which can cause aneuploidy<sup>7,8</sup>. This has parallels to cell division perturbation when cells are exposed to natural or artificial 'long' fibrous material such as asbestos fibers that can induce genomic changes and cancer by sterically blocking cytokinesis<sup>9</sup>.

Understanding how internal mechanical perturbation by internalized particles can affect the cell cycle has relevance not only to fundamental mechanobiology, but also to micro- and nanotoxicity in nanomedicine. However, how intracellular mechanical perturbations alter the cell cycle still remains elusive. Here, we have established how intracellular reinforcements,

hindrance blocking and structural supports on cell membrane induced by internalized physical structures mechanically affect the cell cycle and contribute to cell death.

### 1. Design and fabrication of high aspect-ratio intracellular mechanical drugs

We predicted that internalized mechanical drugs with precisely prescribed shape and dimensions in the range of the cell mitotic diameter ( $\Phi_{HeLa} = 20.9 \pm 0.6 \mu\text{m}$ ) would destabilize cell mechanics during mitosis, allowing us to study intracellular reinforcements and constrains. To assist the internalization of these large objects, we extended our experience in the internalization of smaller polysilicon devices by HeLa cells<sup>10-12</sup> and the fact that many cell types favour 'tip-first' internalization of 1D materials<sup>13</sup>. Accordingly, we designed high aspect-ratio 8-pronged star-shaped devices that mimic 1D structures, measuring  $23.5 \mu\text{m}$  in diameter ( $\Phi$ ) and 500-nm thick ( $t$ ), and comprising cantilevers measuring  $10\text{-}\mu\text{m}$  long ( $L$ ) and  $1.5\text{-}\mu\text{m}$  wide ( $W$ ) (Fig. 1a); we refer to these as SL-500 devices.

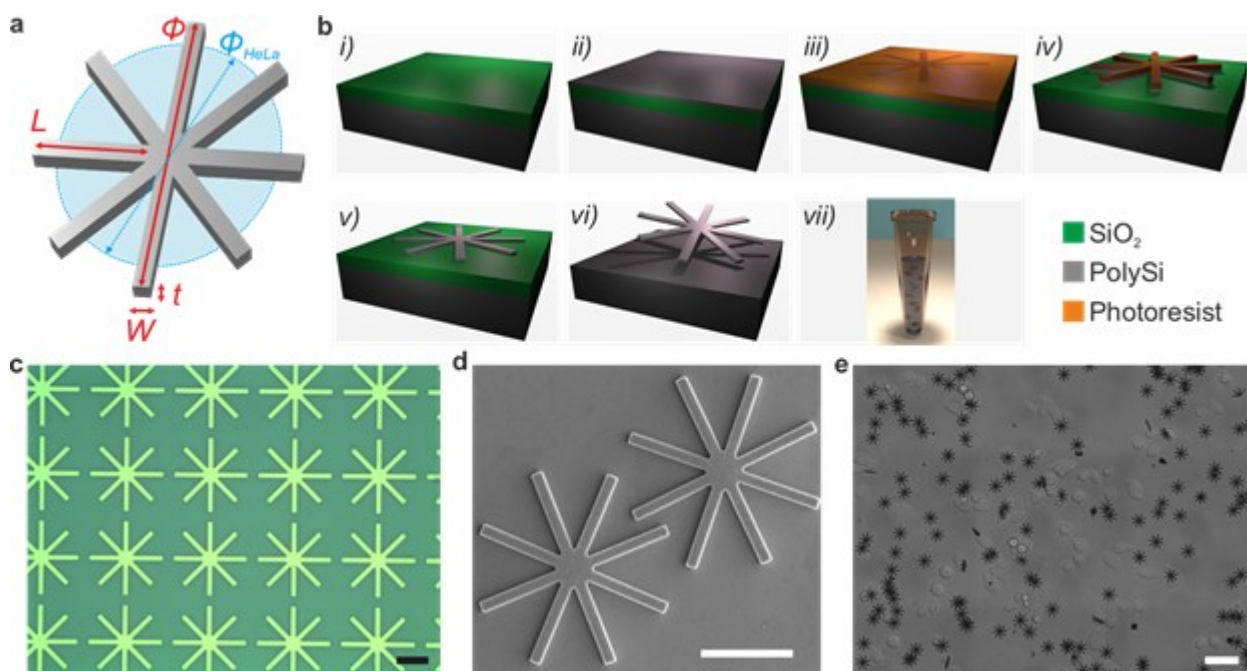


**Figure 1: Design and fabrication of intracellular mechanical drugs.** a, Schematic of the 8-pronged star showing the definition of main geometrical parameters ( $t$  = thickness,  $w$  and  $L$  = cantilever's

width and length,  $\Phi$  = device diameter,  $\Phi_{HeLa}$  = mitotic diameter of a HeLa cell. **b**, Schematic of the technology. **(b,i)** A 1- $\mu\text{m}$ -thick silicon oxide layer (green) is grown on a silicon substrate. **(b,ii)** A polysilicon layer is deposited as a structural layer. **(b,iii)** A photolithographic process defines the shape of the chips. **(b,iv)** Photoresist is striped and polysilicon dry etched to pattern the device. **(b,v)** Photoresist is removed. **(b,vi)** Silicon oxide sacrificial etching to release the chips. **(b,vi)** Released chips are immersed on ethanol and collected in an Eppendorf. **c**, Optical image of the chips at wafer level. **d**, SEM images of the released chips. **e**, Optical images of HeLa cells co-cultured with the devices. Scales bars = **(c, d)** 10  $\mu\text{m}$  and **(e)** 50  $\mu\text{m}$ .

These studies required mass production of biocompatible devices with highly reproducible shape, dimensions and material properties<sup>14</sup>. Following these requirements, we used silicon technologies allowing the fabrication of high-aspect-ratio polysilicon devices that can be precisely patterned at micro- and nanoscales and have been used successfully to probe intracellular mechanical processes<sup>12,15</sup>. Moreover, the inherent biocompatibility of silicon-based devices<sup>16</sup> has allowed the internalization and the microinjection of silicon-based chips by cells and embryos<sup>11,12,15,17</sup>. The fabrication technology is similar to that previously reported for intracellular silicon chips production<sup>10,11</sup>, whose biocompatibility have been proven. Briefly, a 1- $\mu\text{m}$ -thick silicon oxide layer is deposited onto a silicon substrate (Fig. 1b, Supplementary Fig. 1 and Supplementary Methods) as sacrificial layer. Onto this, a structural polysilicon layer is deposited whose thickness defines the thickness of the devices. A photolithographic step and subsequent polysilicon etching patterns the chips (Fig. 1c). Finally, the devices were released from the substrate by etching the sacrificial silicon oxide layer (Fig. 1d) and were collected and suspended in 96% ethanol to prevent the contamination of the samples (Fig. 1b and Supplementary Movie 1). The technology allowed the batch fabrication of more than 7 million identical devices on a 4" silicon wafer. The high geometric reproducibility of the fabricated devices,  $\Phi = 23.27 \pm 0.01 \mu\text{m}$  and  $t = 487.0 \pm 1.2$

nm (Supplementary Fig. 2) allows to circumvent the challenge in studying cell mechanobiology by providing tools with exquisitely well-controlled physical properties.

## 2. High rate of SL-500 devices internalization by HeLa cells

We initially used the human cervical carcinoma HeLa cell line, a model routinely used in human cell biology and cancer research<sup>18</sup>. To facilitate SL-500 internalization, HeLa cells were incubated in small volumes with devices, Fig. 1e, with a minimum cell:device ratio of 2:1 (Supplementary Methods). Notwithstanding a total apparent SL-500 weight of 0.73 pN (Supplementary Fig. 3), we anticipated that HeLa cells would successfully engage with the devices. To analyse cell behaviour thoroughly, we followed the interaction of individual HeLa cells with an associated single SL-500 device in one-to-one mode by time-lapse microscopy (Supplementary Methods).

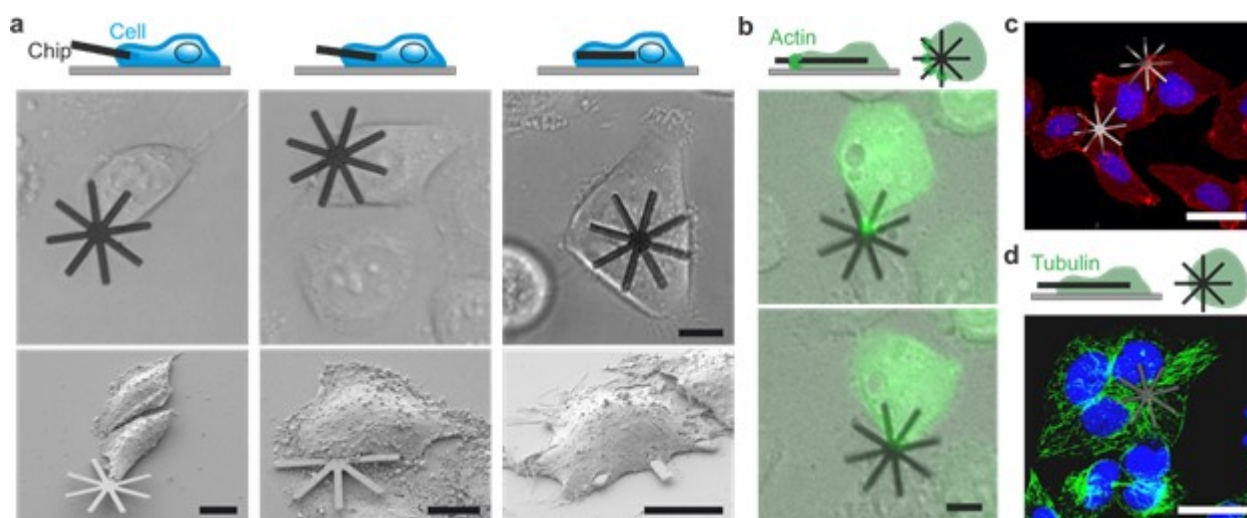


**Figure 2: Device internalization by HeLa.** **a**, Schematic (top), optical images of living HeLa cells (middle) and SEM images (bottom) of fixed cells internalizing SL-500 devices. **b**, Schematic (top) and fluorescence images of HeLa living cells showing actin (green) enrichment in the interaction with SL-500 devices. **c**, Fluorescence images of cell membrane (red) in HeLa fixed cells with internalized SL-500 devices. **d**, Schematic (top) and fluorescence images of  $\beta$ -tubulin (green) in HeLa fixed cells

with internalized SL-500 devices. Cell nuclei are blue in **(c)** and **(d)**. Scales bars = **(a, b)** 10  $\mu\text{m}$  and **(c, d)** 25  $\mu\text{m}$ .

Despite the large diameter of the devices,  $86.51 \pm 5.29\%$  HeLa cells partially or totally internalized nearby devices, typically by catching the proximal arm of the star (Fig. 2a; Supplementary Movie 2), corroborating the prediction that a design sharing features with a 1D structure would show tip-first internalization. We also observed actin-based protrusions extending along the target, a characteristic of phagocytosis<sup>19</sup> (Fig. 2b and Supplementary Movie 3). Recent work suggests that phagocytosis by non-professional phagocytes is a general feature of normal tissue cells<sup>20</sup>. Moreover, plasma membrane surrounded the devices in the places where they pierce the cell (Fig. 2c). Contrary, we found no evidence of direct interaction between the SL-500 devices and microtubules (Fig. 2d), consistent with the behaviour of polysilicon devices microinjected within mouse embryos<sup>15</sup>.

### **3. Intracellular mechanical drugs alter cell division and provoke cell death**

SL-500 internalization altered the cell cycle and ultimately caused cell death (Fig. 3a-c and Supplementary Fig. 4). To characterize this, we followed the behaviour of HeLa cells with partially or totally internalized SL-500 devices for 24 h, a period that includes at least one cell division (HeLa cell doubling time:  $18.0 \pm 0.5$  h). We found that 90.38% of cells with totally internalized SL-500 exhibited the hallmarks of mechanically altered cell cycle (MACC) (Fig. 3d), including 55.32% with delayed or blocked mitosis, 25.53% that failed to execute cytokinesis and 19.15% undergoing asymmetric division (Fig. 3e, Supplementary Fig. 4, 5 and Supplementary Movie 4). During this observation period,  $31.35 \pm 9.98\%$  of HeLa cells with internalized SL-500 died, compared to  $<1\%$  of cells lacking devices (Fig.

3b,c,f and Supplementary Movie 5). This suggests that cell death was a direct consequence of star device internalization and, more often, subsequent MACC.

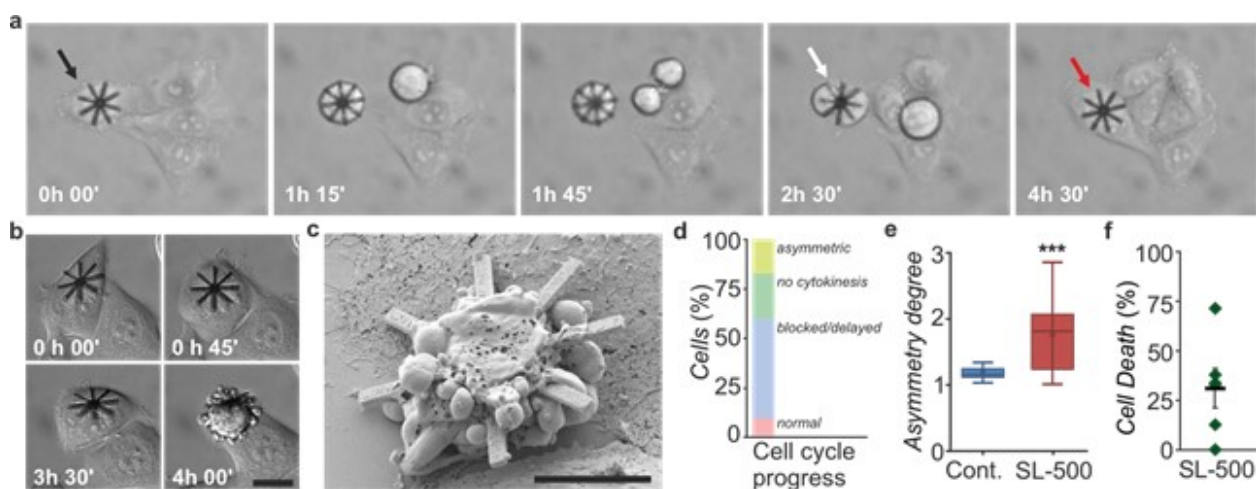


**Figure 3: Intracellular SL-500 promote MACC and cell death on HeLa cells.** **a**, Optical images from a time lapse experiment showing a HeLa cell with an internalized SL-500 device (black arrow) with blocked mitosis (white arrow) and failed cytokinesis (red arrow). The nearby cell divides normally. **b**, Still optical images from a time lapse experiment showing a HeLa cell with an internalized SL-500 device that causes cell death. **c**, SEM image of a dead cell with an internalized SL-500 device. **d**, Percentage of MACC categories of HeLa cells with internalized SL-500 devices. **e**, Mitotic asymmetry induced by internalized SL-500 devices in HeLa cells versus normal cells,  $p = 0.0009$  (Mann Whitney U test). **f**, Cell death percentage of HeLa cells with internalized SL-500 devices. Each dot (**f**) represents an independent experiment where individual cells were followed for 24 h and the outcome plotted (Supplementary Methods). Horizontal black line represents the mean  $\pm$  s.e.m. Scale bars = **(a)** 20  $\mu\text{m}$  and **(b, c)** 10  $\mu\text{m}$ . Total number of analysed cells,  $n = 33-48$ .

### 3.1. Intracellular mechanical device shape is a major determinant of cell damage

We wished to delineate the mechanical basis of the cell cycle interference and cell death induced by the intracellular constrains, reinforcements and supports and we reasoned that perturbation may depend on physical constraint effects on the cytoplasm. To test this

hypothesis, we designed and fabricated devices with varying shape (star (S) and disk (D)) and  $\Phi$  (23.5  $\mu\text{m}$  (L) and 13.7  $\mu\text{m}$  (s)), and with varying thickness (50, 110, 230 and 500 nm) (Fig. 4a and Supplementary Fig. 1,3). Maximal hindrance is predicted for devices with larger diameters and in-plane areas (Fig. 4b).

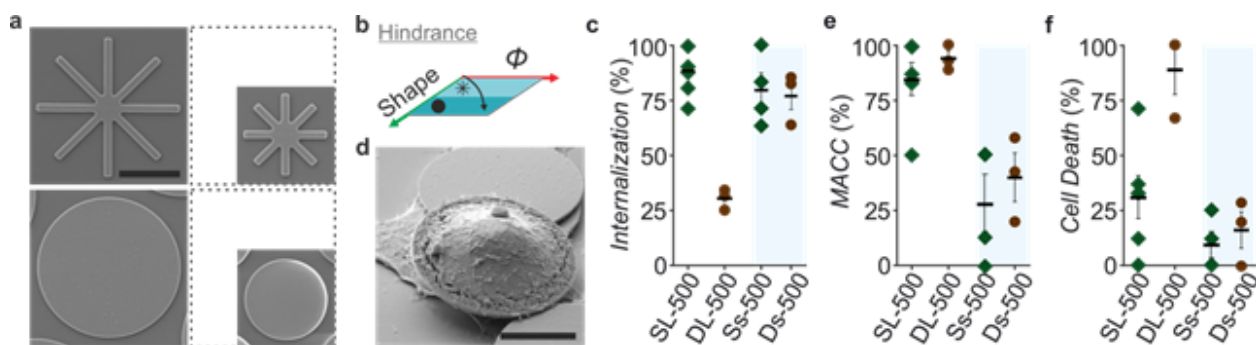


**Figure 4: Hindrance effects in the cytoplasm.** **a**, SEM images of fabricated SL, Ss, DL and Ds devices. **b**, Expected hindrance effects on cells versus shape and  $\Phi$  of the devices. **c**, Internalization rate for all the devices in HeLa cells. **d**, SEM image of a HeLa cell with an internalized DL-500. Percentages of **(e)** MACC and **(f)** cell death of HeLa cells with internalized devices. Each dot **(c, e, f)** represents an independent experiment where individual cells were followed for 24 h and the outcome plotted (Supplementary Methods). Horizontal black lines represent the mean  $\pm$  s.e.m. Scale bars = 10  $\mu\text{m}$ . Total number of analysed cells,  $n = 33-48$ .

Ss-500 and Ds-500 devices exhibited high internalization rates, similar to those of the SL-500 devices ( $76.11 \pm 9.31\%$  and  $73.89 \pm 7.84\%$ , respectively; Fig. 4c and Supplementary Fig. 6). We observed that DL-500, a disk device whose diameter ( $23.45 \pm 0.02 \mu\text{m}$ ) is larger than that of the mitotic radius, were also internalized (Fig. 4d and Supplementary Fig. 6), albeit at a lower frequency than SL-500 ( $18.53 \pm 3.14\%$  vs  $86.51 \pm 5.29\%$ ;  $p=0.0001$ ). Clearly, HeLa cells have difficulties internalizing large 2D disks such as DL-500, and this probably reflects the need for extensive morphological remodelling, as the device surface area represents  $\sim 66\%$

of the cell surface area (Supplementary Fig. 3). Internalization of chips with lateral dimensions of 25  $\mu\text{m}$  has been described for different cell lines<sup>21</sup>. Conversely, on phagocytic cells it has been suggested that the total surface area of the internalized devices, rather than their volume, determines the maximum load due to the additional membrane required for envelopment<sup>22</sup>.

Our results show that HeLa cells favoured the internalization of large devices with features akin to pseudo-1D structures, as with the star design. This suggests that particle shape plays a dominant role in internalization by HeLa cells, a phenomenon also reported in professional phagocytes<sup>23</sup>.

Internalized DL-500 devices exerted major MACC (Fig. 4e), inducing nearly 90% cell death (Fig. 4f). This may reflect their tendency to locate centrally during cell division. By contrast, Ss-500 and Ds-500 devices generated smaller MACC ( $28.00 \pm 12.94\%$  and  $40.40 \pm 11.13\%$ , respectively) (Fig. 4e) and less cell death ( $9.25 \pm 5.96\%$  and  $16.19 \pm 8.46\%$ , respectively; Fig. 4f). During cell division, when these smaller devices located away from the centre, they did not obstruct correct spindle positioning (Supplementary Movie 6). These results show that MACC and cell death due to hindrance effects are minimized if the devices are located away from the cell centre.

However, intracellular hindrance is not only a function of device volume (Supplementary Fig. 3). The volume of Ds-500 devices was  $\sim 31\%$  greater than that of SL-500 even though SL-500 induced  $\sim 94\%$  more cell death (Fig. 4f). The disk-shape devices show higher cell death rates even though they all have the same diameter, DL-500 induced  $\sim 184\%$  more than SL-500 and Ds-500  $\sim 75\%$  more than star-shaped Ss-500. This suggests that device shape, rather than volume or diameter, is a major determinant of intracellular mechanical damage.

### 3.2. Intracellular mechanical device stiffness as dominant factor to alter cell cycle and provoke cell death

We next tested the possibility that intracellular mechanical perturbation also correlated with device stiffness,  $K$ . We predicted that if the device stiffness were sufficiently low, intracellular forces could bend the devices and place them to reduce their mechanical impact on the cell, which is what had happened with relatively small star and disk devices. Experiments that study the elastic component of HeLa cells calculated an effective Young's modulus of  $\sim 30$  kPa<sup>24</sup>, whereas polysilicon has a Young's modulus  $10^6$  times larger ( $\sim 169$  GPa)<sup>25</sup>, which, in principle, suggests that the cells would experience great difficulty in bending internalized devices. However, high aspect ratio devices (Supplementary Fig. 3) had reduced stiffness. For the same diameter, disk-shaped devices stiffness was larger than that of star-shaped, and increased with thickness (Fig. 5a). We fabricated devices with different thickness ( $t = 487.0 \pm 1.2$  nm,  $241.6 \pm 4.0$  nm,  $109.4 \pm 2.0$  nm and  $46.5 \pm 0.4$  nm), for which numerical simulations, by using Finite Element Method (FEM), revealed a wide range of stiffness, from  $19.4 \pm 0.4$  nN/ $\mu$ m for SL-050, to  $(1.17 \pm 0.06) \cdot 10^6$  nN/ $\mu$ m for Ds-500 (Fig. 5b, Supplementary Fig. 7 and Supplementary Methods).

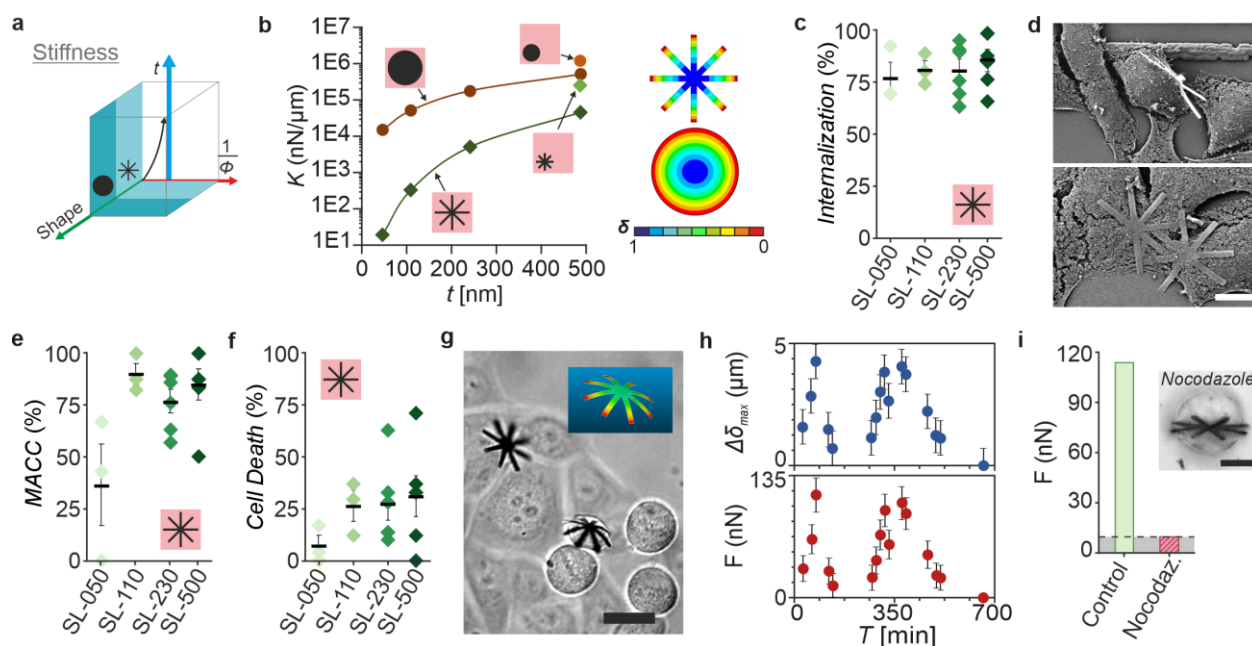


**Figure 5: Stiffness effects in the cytoplasm (I).** **a**, Schematic of stiffness effects on cells versus shape,  $t$  and the  $l/\Phi$  of the devices on cells. **b**, (Left) Finite element simulated stiffness of the devices versus thickness for the star- and disk-shape devices (Force load case). (Right) Normalized  $z$ -displacement of the structures. **c**, Internalization rate in HeLa cells for the SL devices with different thickness. Each dot represents an independent experiment where individual cells were followed for 24 h and the outcome plotted. **d**, HeLa cells internalizing SL-50 devices (Top) by tip-first and (Bottom) parallel showing multiple internalization points with the cell membrane. **e**, Percentages of MACC and **(f)** Cell Death for the SL devices with different thickness. Each dot as in **(c)**. **g**, Still optical image from a time lapse experiment showing a bended SL-050 device internalized inside a HeLa cell. (Inset) A normalized deformation of the device by FEM. **h**, (Top) Increment of device deformation,  $\Delta\delta_{max}$ , versus time,  $T$ , from **(g)** of a SL-050 device inside a HeLa cell and (bottom) corresponding force to achieve  $\Delta\delta_{max}$ . **i**, Maximum intracellular force determined by SL-050 nanodevices for control and nocodazole treated HeLa cells, and optical image of the minimum intensity projection of a SL-050 internalized in a HeLa cell treated with nocodazole. Each dot in **(c, e, f)** represents an independent experiment where individual cells were followed for 24 h and the outcome plotted (Supplementary Methods). Horizontal black lines represent the mean  $\pm$  s.e.m. Scale bars = **(d, i)** 10  $\mu\text{m}$  and **(g)** 20  $\mu\text{m}$ . Total number of analysed cells,  $n = 22 - 99$ .

We evaluated mechanical perturbation induced by internalized large star-shaped (SL) devices of different thickness due to their reduced stiffness compared with the disk-shape devices (Fig. 5b). We found no significant differences among internalization rates at all thickness (Fig. 5c). Most SL devices underwent perpendicular tip-first internalization and, in a minority of cases, planar cell surface internalization, typically for SL-050 devices (Fig. 5d) because their rigidity was small enough to allow bending at multiple points, and hence, more contacts or contacts with a bigger footprint. MACC and cell death (Fig. 5e,f) were clearly smaller for SL-050 devices, which had the lowest stiffness (Fig.5b) and intracellular forces were sufficient to bend them during mitosis (Fig. 5g and Supplementary Movie 7). On the contrary, MACC and cell death caused by thicker SL-110, SL-230 and SL-500 devices were similarly large (Fig. 5e,f) and measurable device bending was not observed. This corroborates that cells cannot generate enough intracellular force to bend SL-110, SL-230 and SL-500 devices to relocate them in a less harmful position. The maximum intracellular mechanical load exerted by cells during mitosis,  $F_{mit\_max}$ , is between  $114 \pm 19$  nN and  $160 \pm 9$  nN, which corresponds to the force to bend the SL-050 devices up to  $4.3 \pm 0.7$   $\mu\text{m}$  (Fig. 5h) and the required force to bend the SL-110 device by  $\geq 0.5$   $\mu\text{m}$  (minimum observable deflection, not detected for SL-110; Supplementary Figure 7), respectively.

Although comparison between studies are thwarted by technical differences, probe size and hierarchical level, our intracellular forces measurements were in agreement with extracellular confinement forces obtained by scanning force microscopy<sup>26</sup>. Mitotic HeLa cells could withstand external confinement forces up to 100 nN before reaching heights that retard mitotic progression and forces over 150 nN blocked mitosis completely due to the mechanical perturbation of spindle geometry<sup>26</sup>. Both values are in agreement with our intracellular measurements indicating that the main force generator during large cell confinement is the spindle apparatus, as our intracellular measurements are not affected

neither by the intracellular hydrostatic pressure<sup>27</sup> nor the reduced surface tension exerted by either the membrane and cortex<sup>28</sup>.

To further demonstrate this reasoning, we performed a molecular perturbation experiment where we used 1- $\mu$ M nocodazole to destabilize microtubules and suppress their polymerization<sup>29</sup>, preventing spindle formation but leading cell rounding<sup>30</sup>. Nocodazole was added after the SL-050 devices were internalized in HeLa cells and we observed that, in the absence of the spindle (Supplementary Fig. 8), the nanodevices did not show an observable bending and hence a reduced intracellular force (Fig. 5i) confirming that spindle and not the membrane-cortex system is the source of the intracellular forces that prevent confinement.

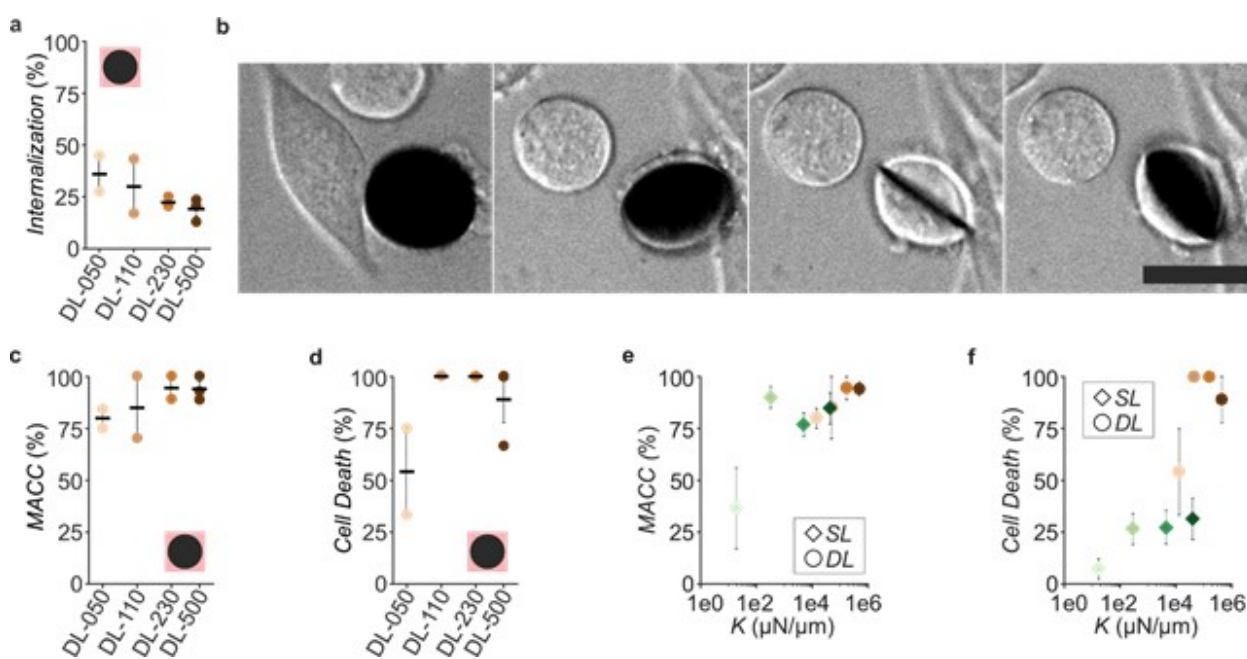


**Figure 6: Stiffness effects in the cytoplasm (II).** **a**, Internalization rate in HeLa cells for the DL devices with different thickness. **b**, Still optical images from a time lapse experiment of a HeLa cell with an internalized DL-500 device. Scale bar = 20  $\mu\text{m}$ . **c**, Percentages of MACC and **(d)** cell death for the DL devices with different thickness. **e**, MACC and **(f)** cell death versus the device stiffness (Force Load model). Each dot in **(a, c-f)** represents an independent experiment where individual cells were followed for 24 h and the outcome plotted (Supplementary Methods). Horizontal black lines represent the mean  $\pm$  s.e.m. Total number of analysed cells,  $n = 22 - 99$ .

Contrary, DL devices exhibited lower internalization rates for all thicknesses compared to star-shaped devices (Fig. 6a), further suggesting that in the 50 to 500 nm range, shape, and not thickness, is the predominant factor for internalization. As with SL devices, DL devices typically occupied an equatorial position during cell division (Fig. 6b), where the spindle would normally be; this is consistent with an average of  $88.29 \pm 3.11\%$  of MACC produced by internalized disks of any thickness (Fig. 6c). Cell death occurred in  $96.30 \pm 3.70\%$  in average of cells containing DL devices  $\geq 110$  nm thick, and  $54.17 \pm 20.83\%$  for DL-050 devices (Fig. 6d). Therefore, only when the device stiffness was sufficiently low to permit device bending during division, MACC and cell death were diminished (Fig. 6e,f). In addition, device shape is relevant to cell death, whose values were always larger for disks, and even in disks of reduced stiffness (DL-050) (Fig. 6f).

### **3.3. Device structural support on cell membrane causes major mitotic perturbation**

Although the volume of a HeLa cell is more than an order of magnitude smaller than the volume of a one-cell mouse embryo, we detected forces almost ten times larger (114 nN vs 17.7 nN, respectively), and 1745 Pa and 233 Pa when expressed in terms of pressure<sup>15</sup>. This led us to consider the role played by structural support of the devices at the cell membrane, understood as the structural support of the cantilevers in the cortex that limits the device displacements.

Mechanical supports at the cell membrane fixed the position of internalized devices larger than the HeLa cell diameter, producing a robust mechanical perturbation during cell division. During mitotic rounding, the devices relocated (Fig. 6b and Fig. 7a,b). DL and SL devices were anchored by fixed supports to the cell membrane. Equivalent boundary condition is exhibited for the SL devices with cantilevers piercing the membrane and taking-off part of

the cantilever, especially the thinnest ones (SL-050). Although individual cantilever supports could act as a roller, the non-parallel cantilever distribution also causes the global fixing of the devices (Fig. 7c and Supplementary Fig. 9). In agreement with this cell expulsion of anchored intracellular devices was not observed in these cases. Thus, devices that exceed the cell diameter can become internalized and immobilized during mitosis. Cell responses to these configurations mimic those induced by cell-internalized meshes of 1D and 2D materials<sup>9</sup>.

We also asked why DL and SL devices tend to position close to the cell equator during division, a positioning that clearly becomes a critical mechanical obstacle for productive mitotic spindle positioning. We propose that centering is a response to multiple phenomena. Actin-mediated internalization would favor internalization perpendicularly to the membrane<sup>13</sup>. Indeed, we observed cortical actin accumulation during internalization in contact with the chips (Fig. 2b). Moreover, the generation of protrusive forces due to surface tension of the membrane-cortex system<sup>19</sup> would also facilitate perpendicular internalization<sup>13</sup>. A simple qualitative Newton formulation, corroborated by FEM, further suggested that if a device is internalized obliquely with respect to the tensioned membrane-cortex system, with different contact angles  $\theta_1$  and  $\theta_2$ , unbalanced forces will be induced that favor perpendicular internalization (Fig. 7d,e, Supplementary Fig. 9 and Supplementary Method). Once internalized, a gradient of effective stiffness (GES) contributes to device centering, further inducing device convergence towards the center, where the cytoplasmic effective stiffness is lower<sup>15</sup> (Fig. 7f and Supplementary Fig. 9).

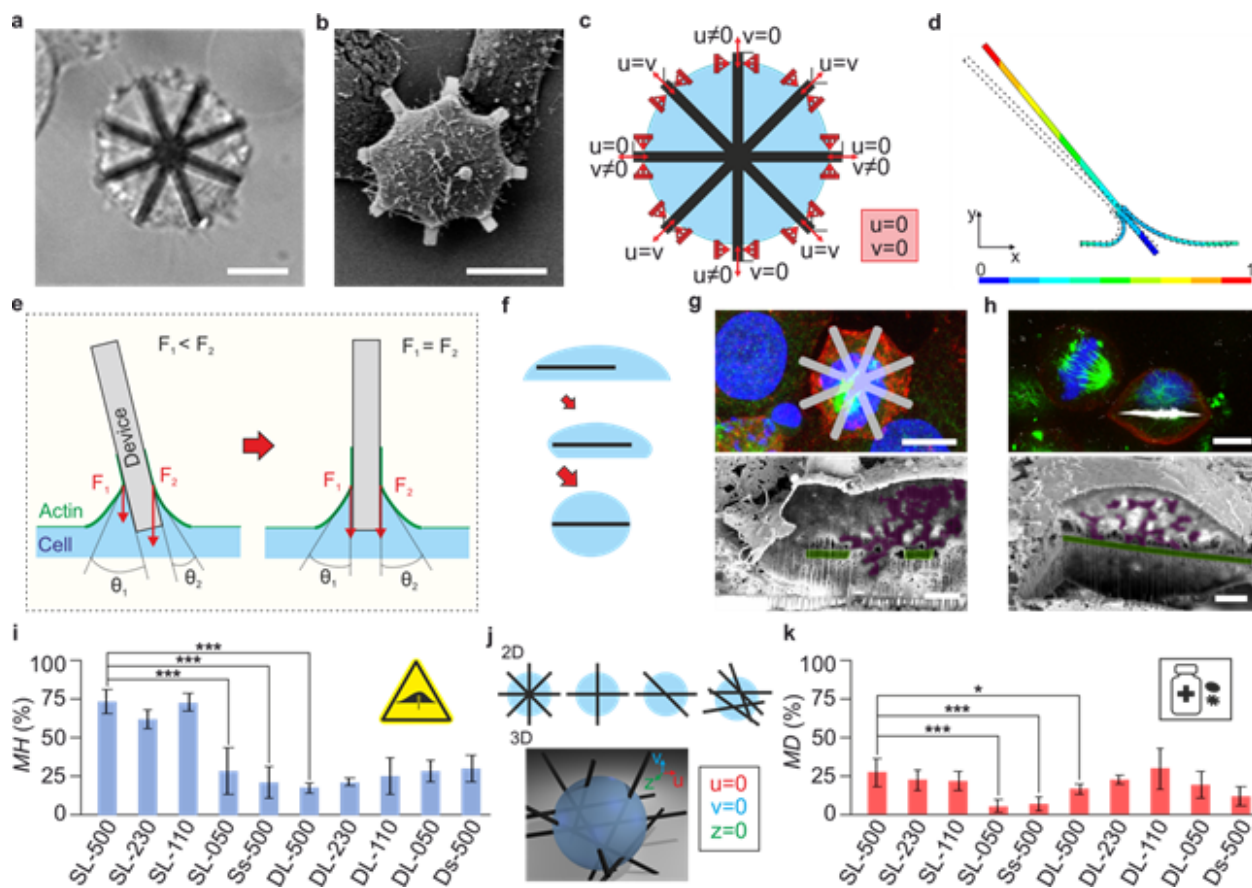


**Figure 7: Maximization of the device mechanical disruption and their application to nanomedicine.** **a**, Optical and **(b)** SEM images of a HeLa cell during mitosis with an internalized and centred SL-500 and SL-050, respectively. **c**, Roller support constrains on the cell membrane for the star-shaped devices fixed the chips during mitosis.  $u$  and  $v$  represent local axis. **d**, A simulated and **(e)** analytical force model based on the surface stress,  $\gamma$ , at the membrane-cortex system favouring perpendicular internalization of the chips. **f**, Gradient of effective stiffness (GES) model favouring cell centering. **g**, **h**, (Top) Confocal images of a cell stained with phalloidin for actin (red), tubulin for microtubules (green) and DAPI for nuclei (blue); (bottom) SEM images of nanomachined cells with internalized **(g)** SL-500 and **(h)** DL-500 chips. **i**, Mechanical Hazard (MH) index for all the devices. **j**, 2D and 3D combination of non-parallel 1D structures which overpass the cell diameter are fixed during mitosis. **k**, Mechanical Death (MD) index for all the devices. Statistical comparisons between groups:  $p < 0.05$ ,  $** < 0.01$  and  $*** < 0.0001$  (Two-tailed Student's t-test). Scale bars = **(a,b,top-g,top-h)** 10  $\mu\text{m}$  and **(bottom-g, bottom-h)** 1.5  $\mu\text{m}$ .

Overall, the tendency of the devices to be located at the cell equator during cell-rounding is predicted to hinder spindle centering and chromosome alignment, both of which are essential for normative cytokinesis<sup>31</sup>. We accordingly observed spindles and the chromosomes intertwined with the arms of SL designs (Fig. 7g). DL devices apparently excluded the spindle and chromosomes to one of the cell hemispheres (Fig. 7h, Supplementary Fig. 10 and Movie 8). Even if the spindle can be mounted in one hemisphere (Fig. 7h,top and Supplementary Fig. 10), the cell division would be compromised as it is taking place in a confined space<sup>26,31–33</sup>.

#### 4. Intracellular mechanical drugs towards nanomedicine

Internalization rates, MACC and cell death are parameters that should be considered together when evaluating the toxicity of physical objects or their future use as physical drugs. When cells are exposed to mechanical objects, the damage they undergo reflects both their capacity to internalize them and their intracellular consequences. To assess this, we defined a 'Mechanical Hazard (MH)' index by multiplying the internalization rate for each device and its associated MACC. This suggests that large, stiff, star-shaped devices have the largest MH indices (Fig. 7i), due to relatively large internalization rates (Fig. 4c, Fig. 5c and Fig. 6a). This could be extended to demonstrate the potential mechanical toxicity of materials composed of meshes of 1D structures, such as nanofibers (*i.e.* asbestos), nanowires, or 2D and 3D materials with parts of their geometry that mimic 1D structures (Fig. 7j) and may facilitate internalization, whilst meshes increase the stiffness and anchor the structure to the cortex. In spite of the strong MACC effects of large disk devices, because their internalization rate is low, their MH indices are low and comparable to those of disks and stars with smaller diameter. Barriers to internalizing larger structures are presumably a constitutive mechanism to avoid a large intracellular mechanical toxicity. However, large 2D

structures with parts that resemble 1D structures are clearly able to circumvent this barrier and elicit increased mechanical toxicity.

Notwithstanding considerable research effort, there remains a lack of cell mechanics applications to biomedicine in a manner that is analogous to chemical drugs. Mechanical devices acting as physically- rather than chemically-based drugs could meet criteria required of functional biomaterials designed to steer cell fate and function in prescribed directions<sup>34</sup>. With this in mind, it may be possible to evaluate devices as mechanical agents that kill cells. To achieve this, we propose a mechanical death index,  $MD = \text{internalization rate} \times \text{cell death rate}$ . Outstandingly, MD is similar for SL-500 and DL-500 devices (Fig. 7k), yet with higher cell death rates for the latter (Fig. 4f, Fig. 5f and Fig. 6d). Anyway, devices have to be stiff enough to increase their cell-killing capability by interfering in the spindle localization and mounting (Fig. 7k). Remarkably, it has to be considered that most surviving cells with blocked mitosis or failed cytokinesis could die after the last observational time-point (Supplementary Movie 9). Thus, these results suggest a potential application of the mechanical drugs to kill cells, which will require studies covering longer times to evaluate the fitness of daughter cells.

## Discussion

Current advances in materials science have demonstrated that extracellular mechanical cues can define cell function and cell fate; here we determined how intracellular mechanical cues produce similar effects. We have shown that the use of highly reproducible intracellular nanomechanical drugs that can be precisely tuned in shape, dimensions and stiffness, allow the study of how intracellular physical structures interfere mechanically with cell function, contributing to better understanding cell physiology and disease.

In this context, our results show that non-phagocytic HeLa cells can internalize nanostructures with diameters that exceed their mitotic diameter and those with parts akin to 1D structures are more easily internalized. In the case of phagocytic cells, there is controversy about their capacity to sense size, shape and rigidity of the engulfed target<sup>22</sup>. For HeLa cells, the predominant parameters guiding internalization are shape and diameter, with almost no effect of thickness in the range 50 nm to 500 nm. This agrees with previous studies on HeLa cells using smaller particles, of *ca.* 5  $\mu\text{m}$  diameter<sup>35</sup>. On the contrary, no significant dependence for uptake efficiency on target rigidity is observed (Fig. 5b,c and Supplementary Fig. 7). It is important to distinguish between global device rigidity, which can be low, and their local rigidity due to the high Young's modulus of polysilicon ( $Y_{\text{polysilicon}} = 169 \text{ GPa}$ ), which is too high for molecular forces to locally deform polysilicon and hence beyond the mechanosensitive range of the cell<sup>22</sup>.

Our results also show that intracellular structures exceeding the HeLa cell diameter were fixed at the cell membrane-cortex system during mitosis and physically tend to occupy the equator during spindle formation and chromosome alignment. These results could be extrapolated to any combination of non-parallel internalized 1D nanostructures that are able to form a 2D or 3D mesh exceeding the mitotic diameter, in which the overall mechanical

boundary conditions can be reduced to zero displacements (Fig. 7c,j). In these cases, nanomeshes formed by 1D nanomaterials (*i.e.* bundles of fibres), would exhibit increased nanotoxicity, as the internalization is favoured by the individual long nanostructures, but rigidity once inside cells is increased by the entanglement of individual 1D structures and by the boundary conditions at the cell membrane-cortex system.

Structures smaller than the cell diameter or with a stiffness below a certain magnitude can be displaced or deformed inside the cell to positions far from the spindle mounting and chromosome alignment, and consequently reduce the MACC and the cell death. Conversely, control and nocodazole treated HeLa cells with nanodevices report that spindle formation is able to generate limited forces, up to 114 nN, to reduce intracellular mechanical confinement. This value is similar to the reported extracellular force of 150 nN to block mitosis due to the mechanical perturbation of spindle geometry on HeLa cells<sup>26</sup>. This agreement indicates that the main force generator during extracellular cell confinement is the spindle apparatus and demonstrates that intracellular chips complement extracellular techniques in order to study the hierarchy of forces in cell mechanics.

The results can go beyond HeLa cell line, as additional cell types exhibited device internalization and affectation (Supplementary Figure 11). The fabrication technology offers the possibility to fabricate devices with different shapes and dimensions in order to better understand universal cell internalization, mechanical affectation on cell cycle and cell death and to avoid or promote devices as drug delivery carriers<sup>23,36</sup>.

The results presented here also provide new insights into future mechanical therapeutics. By the design and reproducible manufacture of precision devices able to perform prescribed intracellular functions, including the induction of cell death or differentiation. Although, the cell-specific delivery may be a challenge, the mass production of mechanical drugs could be

used to kill cancer cells, being their topical use an initial opportunity to explore. While cytokinetic failure can also promote tumorigenesis, the relative chromosomal instability and more rapid division of cancer cells may amplify the effect of mechanical drugs upon them.

To conclude, in contrast to extracellular mechanical tools, internalized mechanical drugs induce an alteration of intracellular boundary conditions, which redistributes the internal cell force balance and induces a rearrangement of the cell mechanical elements. Such intracellular mechanical drugs promise a wide range of possible developments to open new avenues of fundamental study, for instance by mechanically controlling gene regulation or cell differentiation<sup>37</sup>, but also, understanding how intracellular chips affect the cells will pave the way to new therapeutic options. The results show that intracellular chips are an innovative contribution to the semiconductor field as intracellular mechanical sensors, but also as intracellular actuators.

### **Acknowledgments**

The authors are grateful to A. C. F. Perry for his constructive comments during manuscript preparation. This work was supported with funds from the Spanish Government Grant TEC2017-85059-C3, PID2020-115663GB-C3, and by the EU ERDF (FEDER). The authors thank the clean-room staff of IMB-CNM for fabrication of the microparticles and A. Sánchez for the nanomachining of the cells. The authors at CIB Margarita Salas are deeply indebted with the “Confocal Laser and Multidimensional Microscopy in vivo” in-house facility for their excellent work and professional collaboration.

## References

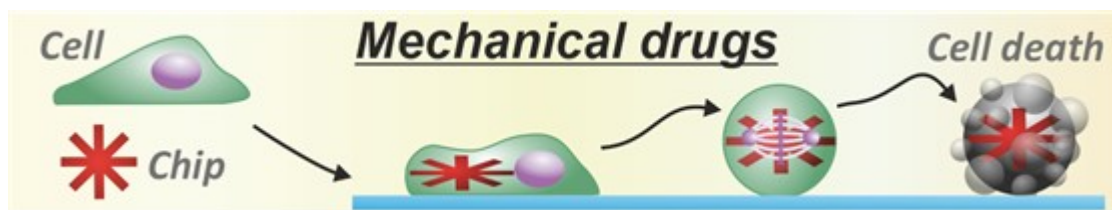
1. Ingber, D. E., Wang, N. & Stamenović, D. Tensegrity, cellular biophysics, and the mechanics of living systems. *Reports on Progress in Physics* vol. 77 (2014).
2. Fletcher, D. A. & Mullins, R. D. Cell mechanics and the cytoskeleton. *Nature* vol. 463 485–492 (2010).
3. Meng, Z., Moroishi, T. & Guan, K. L. Mechanisms of Hippo pathway regulation. *Genes and Development* vol. 30 1–17 (2016).
4. Jordan, M. A. & Wilson, L. MICROTUBULES AS A TARGET FOR. *nature.com* **4**, (2004).
5. Zhou, D. *et al.* Study on the Mutagenesis of Protoplasts from Taxol-producing Fungus *Nodulisporium sylviforme*. *J. Am. Sci.* **1**, 55–62 (2005).
6. Trendowski, M. Exploiting the cytoskeletal filaments of neoplastic cells to potentiate a novel therapeutic approach. *Biochimica et Biophysica Acta - Reviews on Cancer* vol. 1846 599–616 (2014).
7. Janssen, A. & Medema, R. H. Entosis: Aneuploidy by invasion. *Nat. Cell Biol.* **13**, 199–201 (2011).
8. Krajcovic, M. *et al.* A non-genetic route to aneuploidy in human cancers. *Nat. Cell Biol.* **13**, 324–330 (2011).
9. Jensen, C. G., Jensen, L. C. W., Rieder, C. L., Cole, R. W. & Ault, J. G. Long crocidolite asbestos fibers cause polyploidy by sterically blocking cytokinesis. *Carcinogenesis* **17**, 2013–2021 (1996).
10. Fernandez-Rosas, E. *et al.* Intracellular polysilicon barcodes for cell tracking. *Small* **5**,

- 2433–2439 (2009).
11. Gómez-Martínez, R. *et al.* Intracellular silicon chips in living cells. *Small* **6**, 499–502 (2010).
  12. Gómez-Martínez, R. *et al.* Silicon chips detect intracellular pressure changes in living cells. *Nat. Nanotechnol.* **8**, 517–521 (2013).
  13. Shi, X., Von Dem Bussche, A., Hurt, R. H., Kane, A. B. & Gao, H. Cell entry of one-dimensional nanomaterials occurs by tip recognition and rotation. *Nat. Nanotechnol.* **6**, 714–719 (2011).
  14. Shao, Y. & Fu, J. Integrated micro/nanoengineered functional biomaterials for cell mechanics and mechanobiology: A materials perspective. *Advanced Materials* vol. 26 1494–1533 (2014).
  15. Duch, M. *et al.* Tracking intracellular forces and mechanical property changes in mouse one-cell embryo development. *Nat. Mater.* **19**, 1114–1123 (2020).
  16. Fan, J. & Chu, P. K. Group IV nanoparticles: Synthesis, properties, and biological applications. *Small* vol. 6 2080–2098 (2010).
  17. Torras, N. *et al.* Suspended Planar-Array Chips for Molecular Multiplexing at the Microscale. *Adv. Mater.* **28**, 1449–1454 (2016).
  18. Masters, J. R. HeLa cells 50 years on: The good, the bad and the ugly. *Nature Reviews Cancer* vol. 2 315–319 (2002).
  19. Jaumouillé, V. & Waterman, C. M. Physical Constraints and Forces Involved in Phagocytosis. *Frontiers in Immunology* vol. 11 (2020).
  20. Seeberg, J. C. *et al.* Non-professional phagocytosis: a general feature of normal tissue

- cells. *Sci. Rep.* **9**, (2019).
21. Yang, M. X., Hu, X., Akin, D., Poon, A. & Wong, H. S. P. Intracellular detection and communication of a wireless chip in cell. *Sci. Rep.* **11**, (2021).
  22. Vorselen, D. *et al.* Microparticle traction force microscopy reveals subcellular force exertion patterns in immune cell–target interactions. *Nat. Commun.* **11**, (2020).
  23. Champion, J. A. & Mitragotri, S. Role of target geometry in phagocytosis. *Proc. Natl. Acad. Sci. U. S. A.* **103**, 4930–4934 (2006).
  24. Leporatti, S. *et al.* Cytomechanical and topological investigation of MCF-7 cells by scanningforce microscopy. *Nanotechnology* **20**, 55103 (2009).
  25. Sharpe, W. N., Yuan, B., Vaidyanathan, R. & Edwards, R. L. Measurements of Young’s modulus, Poisson’s ratio, and tensile strength of polysilicon. in *Proceedings of the IEEE Micro Electro Mechanical Systems (MEMS)* 424–429 (1997).  
doi:10.1109/memsys.1997.581881.
  26. Cattin, C. J. *et al.* Mechanical control of mitotic progression in single animal cells. *Proc. Natl. Acad. Sci. U. S. A.* **112**, 11258–11263 (2015).
  27. Stewart, M. P. *et al.* Publisher Correction: Hydrostatic pressure and the actomyosin cortex drive mitotic cell rounding (Nature, (2011), 469, 7329, (226-230), 10.1038/nature09642). *Nature* vol. 571 E5 (2019).
  28. Chugh, P. *et al.* Actin cortex architecture regulates cell surface tension. *Nat. Cell Biol.* **19**, 689–697 (2017).
  29. Lu, J. A Quantitative Study of Nocodazole’S Effect on HeLa Cells’ Growth Rate and F-actin Structure. *Am. J. Life Sci.* **6**, 7 (2018).

30. Vasquez, R. J., Howell, B., Yvon, A. M. C., Wadsworth, P. & Cassimeris, L. Nanomolar concentrations of nocodazole alter microtubule dynamic instability in vivo and in vitro. *Mol. Biol. Cell* **8**, 973–985 (1997).
31. Cadart, C., Zlotek-Zlotkiewicz, E., Le Berre, M., Piel, M. & Matthews, H. K. Exploring the function of cell shape and size during mitosis. *Developmental Cell* vol. 29 159–169 (2014).
32. Lancaster, O. M. *et al.* Mitotic Rounding Alters Cell Geometry to Ensure Efficient Bipolar Spindle Formation. *Dev. Cell* **25**, 270–283 (2013).
33. Tse, H. T. K., Weaver, W. M. C. & Carlo, D. Increased asymmetric and multi-daughter cell division in mechanically confined microenvironments. *PLoS One* **7**, (2012).
34. Darnell, M. & Mooney, D. J. Leveraging advances in biology to design biomaterials. *Nature Materials* vol. 16 1178–1184 (2017).
35. Gratton, S. E. A. *et al.* The effect of particle design on cellular internalization pathways. *Proc. Natl. Acad. Sci. U. S. A.* **105**, 11613–11618 (2008).
36. Stewart, M. P. *et al.* In vitro and ex vivo strategies for intracellular delivery. *Nature* vol. 538 183–192 (2016).
37. Panciera, T. *et al.* Reprogramming normal cells into tumour precursors requires ECM stiffness and oncogene-mediated changes of cell mechanical properties. *Nat. Mater.* (2020) doi:10.1038/s41563-020-0615-x.

[Short Text for the Journal's Table of Contents \(ToC\)](#)



Silicon-based chips, larger than cell mitotic diameter, are established for the first time as intracellular mechanical drugs. Once internalized, these tools disrupt the correct development of the cell inducing mechanical affection of the cell cycle and cell death. The intracellular mechanical drugs allow to study how intracellular mechanical cues define cell function with relevance to fundamental cell mechanics and nanomedicine.